

# Automated detection of new impact sites on Martian surface from HiRISE images

Xin Xin<sup>a,b</sup>, Kaichang Di<sup>a</sup>, Yexin Wang<sup>a</sup>, Wenhui Wan<sup>a,\*</sup>, Zongyu Yue<sup>a</sup>

<sup>a</sup> State Key Laboratory of Remote Sensing Science, Institute of Remote Sensing and Digital Earth, Chinese Academy of Sciences, No. 20A, Datun Road, Chaoyang District, Beijing 100101, China

<sup>b</sup> University of Chinese Academy of Sciences, Beijing 100049, China

Received 13 February 2017; received in revised form 19 May 2017; accepted 22 June 2017

Available online 1 July 2017

## Abstract

In this study, an automated method for Martian new impact site detection from single images is presented. It first extracts dark areas in full high resolution image, then detects new impact craters within dark areas using a cascade classifier which combines local binary pattern features and Haar-like features trained by an AdaBoost machine learning algorithm. Experimental results using 100 HiRISE images show that the overall detection rate of proposed method is 84.5%, with a true positive rate of 86.9%. The detection rate and true positive rate in the flat regions are 93.0% and 91.5%, respectively.

© 2017 Published by Elsevier Ltd on behalf of COSPAR.

**Keywords:** New impact sites; Martian surface; HiRISE; Automatic detection; AdaBoost; Machine learning

## 1. Introduction

New impact sites on the Martian surface are the freshest features caused by impacts. On high-resolution images, a new impact site on Mars appears as one single crater or a crater cluster surrounded by large areas of dark region (e.g., Fig. 1). In most dust-mantled regions, the ejecta of new impact craters presents a low albedo (Malin et al., 2006). With the advent of high-resolution images from the Mars Orbiter Camera (MOC, Malin et al., 2010), Thermal Emission Imaging System (THEMIS, Zurek and Smrekar, 2007), Context Camera (CTX, Malin et al., 2007), High-Resolution Imaging Science Experiment (HiRISE, McEwen et al., 2007), and continuing repeat coverage of Mars year by year, more new impact sites have been found (Daubar et al., 2013; Malin et al., 2006). More than 400 new impact sites have been identified on Mars from

2006 to 2014 (Daubar et al., 2014). Study of new impact sites is critical for many geologic processes and to determine ongoing surface changes, such as interpreting the initial impact process (Daubar et al., 2016), studying Martian ground ice (Byrne et al., 2009; Dundas et al., 2014), studying the production of small craters (Williams et al., 2014), and many other studies (Calef III et al., 2009; Golombek et al., 2010).

In previous studies, new impact sites have been primarily extracted by manual identification, which is usually time-consuming. As a vast amount of high-resolution images have been and will continue to be acquired by multiple missions, there is a compelling need to extract new impact sites in an automated way. Recently, several attempts were made to detect new impact sites using automatic change detection methods from high resolution images taken at different times by the same or different orbiters (Wagstaff et al., 2012). However, change detection methods require multi-temporal coverage of the same areas, which is not applicable for many places where only

\* Corresponding author.

E-mail address: [wanhwh@radi.ac.cn](mailto:wanhwh@radi.ac.cn) (W. Wan).

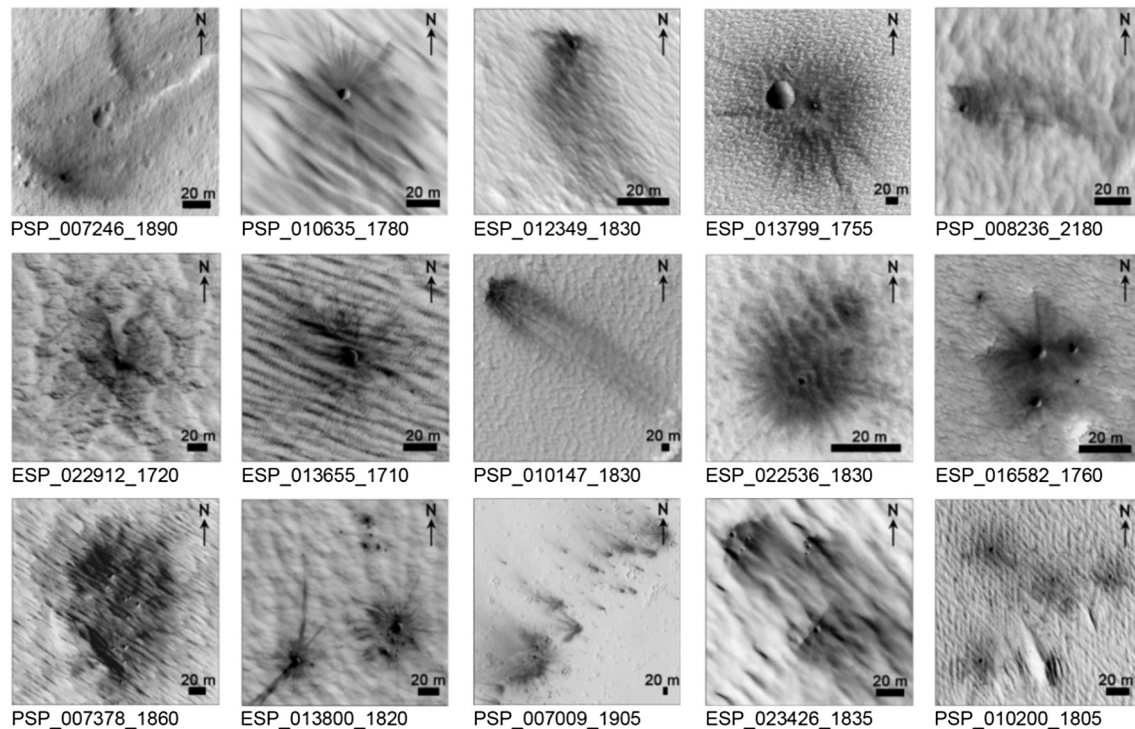


Fig. 1. Examples of new impact sites on Mars (see supplementary material in [Daubar et al., 2013](#)). All of the examples are selected from HiRISE images used in our experiment. Subfigures in row one and the first three ones in row two are examples of new impact sites with a single crater, and the last seven subfigures are examples of new impact sites with crater cluster. HiRISE observation IDs are indicated below each subfigure. All the subfigures are stretched for contrast enhancement. (Image credit: NASA/JPL/University of Arizona).

single coverage of high-resolution images is available. For solving the above problem, we found that most of the new impact sites in dust areas have low albedos, comparing to the bright Mars regolith in dust area. This characteristic can facilitate the identification of new impact sites in dust area. In addition, the low albedo will fade or disappear in short time which also favors new impact site detection in only one image. Considering the above premises and manual identification of a new impact site can be done using single high-resolution images, it is possible to detect new impact sites from these images automatically. An automated method would improve the efficiency for new impact site detection and contribute to the study of impact-ing processes.

In the last decade, numerous automated algorithms have been developed to detect craters from images or digital elevation models ([Salamunićar et al., 2011](#)). Typical algorithms include curve fitting ([Salamunićar et al., 2014](#)), highlight and shadow region matching ([Urbach and Stepinski, 2009](#)), template matching ([Bandeira et al., 2007](#)), machine learning ([Bandeira et al., 2012](#); [Jin and Zhang, 2014](#); [Kim et al., 2005](#); [Martins et al., 2009](#)), and object-oriented methods ([Yue et al., 2008](#)). All of these algorithms are dedicated to detect conventional and relatively large craters. As new impact craters are rare, relatively small, and have surrounding blast zones, these existing algorithms may need modification or improvement in order to effectively detect the new craters or the new impact sites. Particularly, the image characteristics of the

new impact craters (e.g., the visible blast zones) should be considered so as to improve the detection rate and reduce the false positive rate.

In this study, we present an automated method for new impact sites detection from high-resolution images by combining dark-area extraction and crater detection. Sophisticated machine learning techniques have been developed for optimizing crater detection. The dark-area extraction step detects candidates of new impact sites in a full HiRISE image. The machine learning step detects small new crater inside a candidate site to determine if the site is a new impact site. We adopt the AdaBoost machine learning algorithm and also propose cascading two effective image-based features: Local Binary Pattern (LBP) and Haar-like features, to make our method more effective. We verify the proposed method using a large number of high resolution images acquired by HiRISE, which is a representative high resolution imager in Mars missions. Currently, the automated method may not be able to replace human experts for identification and confirmation of new impact sites, it can be useful as a prescreen tool to help improve the efficiency of finding new impact sites.

## 2. Data

HiRISE is a scientific imaging instrument onboard Mars Reconnaissance Orbiter (MRO) that offers ultra-high resolution up to 0.25 m/pixel ([Mcewen et al., 2007](#)). Since 2006, HiRISE has acquired more than forty-eight thousand

images (<http://hirise.lpl.arizona.edu/anazitisi.php>), which have been widely used to investigate impact cratering, volcanology, tectonism, fluvial, and other processes in unprecedented detail.

We selected 132 grayscale (red band) HiRISE images (100 test images and 32 training images, Appendices A), each of which covers at least one new impact site from the list summarized in Daubar et al. (2013) to test our method. The images were downloaded from the HiRISE website (<http://www.uahirise.org/>) in JP2 format and converted to TIFF format.

### 3. Method

In our method, new impact sites are detected from single HiRISE image through dark area extraction and AdaBoost classification. The flowchart of the proposed method is shown in Fig. 2. It consists of the following steps: (1) detect new impact site candidates in every full HiRISE images repeatedly by dark area extraction and morphological processing; (2) extract Haar-like features and LBP features from the sample data, and train the AdaBoost classifier with a cascade of the features using sample data of new impact craters, this step is done only once in the whole experiment; and (3) detect new impact craters inside every candidate site using the AdaBoost classifier constructed in step (2). As a result, the dark areas containing one or more

new impact craters are recognized as new impact sites. Key algorithms of the method are given below in more detail.

#### 3.1. Detection of new impact site candidates

The first step of the proposed method is to detect candidates of new impact sites in full HiRISE images through dark area extraction and morphological processing. All the images are pre-processed by resampling to 2 m and histogram equalization (i.e. spreading out the most frequent intensity values from the histogram) to ensure the consistency of the following experiments with different images. Due to the brightness contrast caused by bright Mars regolith and low albedo ejecta of new impact crater, dark areas becomes the visual cues of candidate impact sites. A dark area consists of connected dark pixels that are extracted using the following formula:

$$D(x,y) = \begin{cases} 1, & \text{if } S = M(x,y) - P(x,y) > T_1 \text{ and } P(x,y) < T_2 \\ 0, & \text{otherwise} \end{cases} \quad (1)$$

where  $P(x,y)$  is the gray scale value (256 values for our eight-bit images) of the pixel at  $(x,y)$  location,  $M(x,y)$  is the mean value of the pixels within a square window centered at  $(x,y)$  with a width  $w$ ,  $S$  is the difference between the mean gray scale value within the window and the cur-

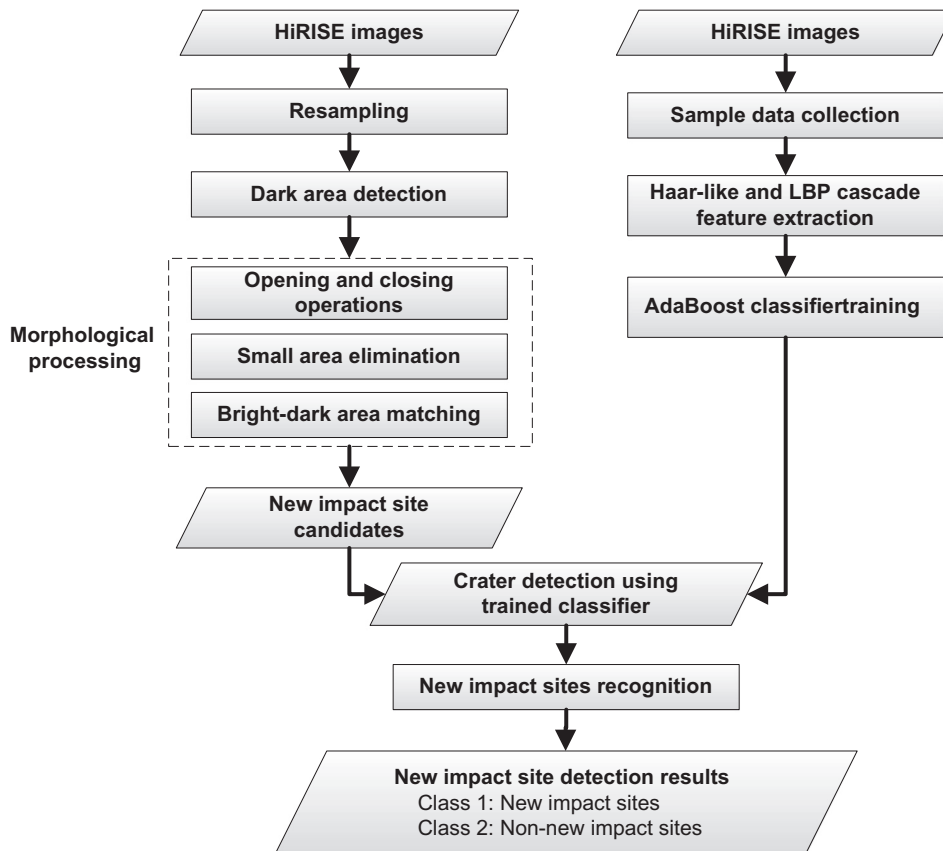


Fig. 2. Flowchart of the proposed method for new impact site detection.

rent pixel  $(x, y)$ ,  $T_1$  and  $T_2$  are pre-defined thresholds. If  $S$  is greater than  $T_1$  and  $P(x, y)$  is less than  $T_2$ , the pixel is marked as a dark pixel. We set  $w$  to be 300 pixels, which is larger than the width of all the new impact sites in our study.  $T_1$  and  $T_2$  are set to be 60 and 90 respectively for all images in the experiments. After computation of all the pixels, dark pixels (with pixel value 1) in an eight-neighborhood are connected to form a dark area. Each dark area is represented as a binary image with dark pixels being the value 1 and background pixels being the value 0.

The dark areas extracted by Eq. (1) may include new impact sites, shadows caused by crater rims, mountain ridges and rocks, or other dark features, such as dark slope streaks and dust devil streaks. In order to eliminate those dark areas that are not related to new impact craters, a series of morphological operations, including opening (erosion operation first, then dilation operation based on mathematical morphology) and closing (dilation operation first, then erosion operation, Serra, 1982), small area elimination and bright-dark area matching, are applied to all the dark areas. First, dark area images are processed by opening and closing operations to remove noise and fill small holes. A disk-shaped structure element with radius of 2 pixels is used in both opening and closing operations. Then, to eliminate narrow and long dark areas (which may be dark slope streaks or shadows caused by mountain ridges), a ratio is calculated as follows:

$$r = \frac{a - b}{a + b} \quad (2)$$

where  $a$  and  $b$  are respectively the maximum and minimum distances between the dark region's edge point and its mass center. Dark areas are retained if  $r$  (the range is 0–1) is less than 0.8 and its area is larger than 200 pixels. Finally, shade regions are filtered out by a bright-dark area match-

ing method (Sawave et al., 2006). A dark area is recognized as a shade area if there is a close-by bright region that has similar shape aligned with the subsolar azimuth as the dark region. In our experiments, we set the threshold of distance between the centroid of bright and dark region as 100 pixels, set the threshold of area difference as 1/3 of the area of dark region, and set the threshold of angle of the two regions as 35 degree. See Fig. 3 for a schematic of bright-dark matching. Fig. 4 shows the intermediate results of new impact site candidate detection.

### 3.2. Training data collection and feature extraction

Most of the new impact blast zones contain one crater or a cluster of small craters. Therefore, the existence of small craters in the extracted dark area is the criterion to determine whether a dark area is a new impact crater site. The craters inside the dark areas are to be detected by an AdaBoost classifier (Viola and Jones, 2004). To train the classifier, we collect square image blocks which contain small craters in dark areas from original HiRISE images as positive sample data. The image blocks are centered on the small craters and having dimensions 1.5 times the diameters of the craters. Considering the image resolution (0.25 m/pixel), only the craters with a diameter greater than 2.0 m are selected as positive samples. The negative samples are randomly selected to be square image blocks containing no new impact crater. The sample data is selected from 32 HiRISE images that are different from the 100 images for testing of the classifier. All of the positive and negative samples are resized (using a bilinear interpolation method) from their original size to a standard size of  $15 \times 15$  pixels. Fig. 5 shows some of the positive and negative samples. To avoid the effects of illumination direction, each sample image block is rotated with angles of

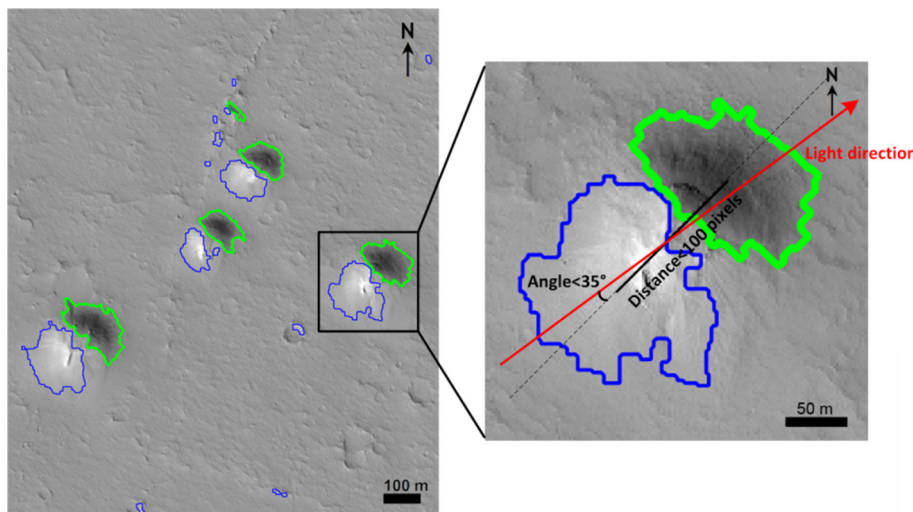


Fig. 3. A schematic illustration of bright-dark matching method. The figure on the left shows four shadow areas that are eliminated by the bright-dark matching method. The blue lines are the boundaries of bright areas, and the green lines are the boundaries of dark areas. The figure on the right is a detailed illustration of this method. (HiRISE observation ID: ESP\_022964\_1845). (For interpretation of the references to colour in this figure legend, the reader is referred to the web version of this article.)

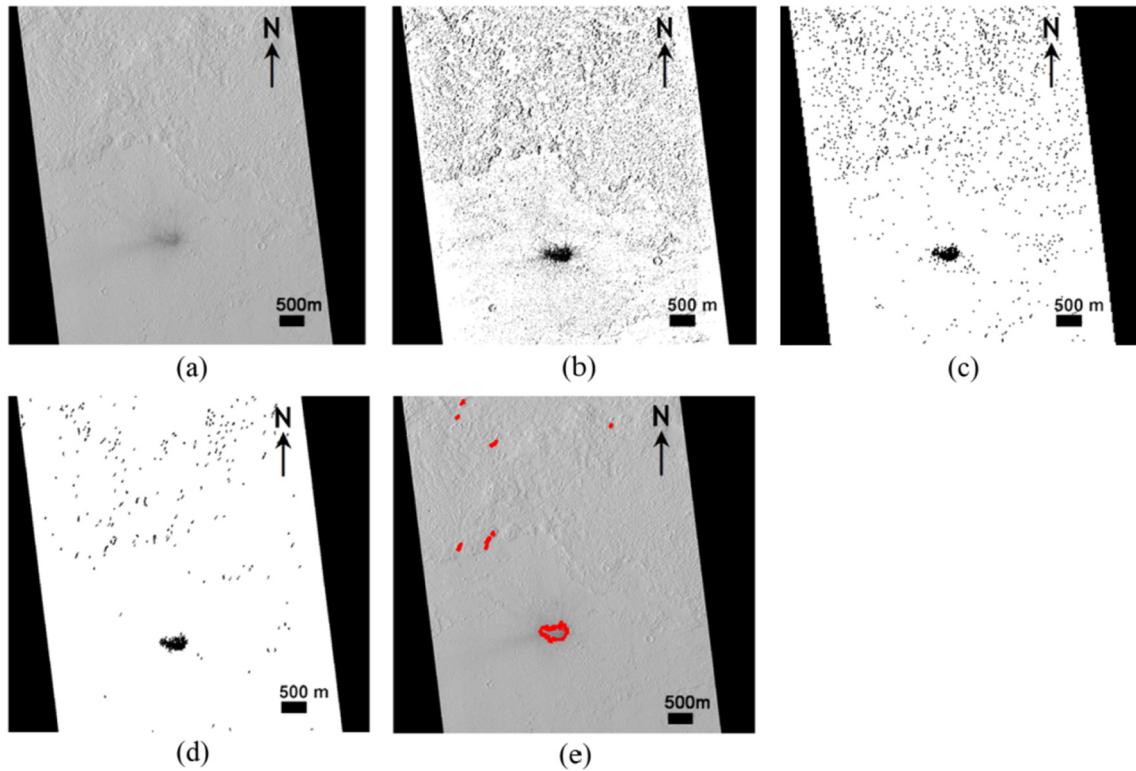


Fig. 4. Intermediate results of new impact site candidate detection. (a) an original image; (b) dark area extraction result; (c) result after opening and closing operations; (d) result after small area elimination; (e) the result after shade area elimination through bright-dark area matching. (HiRISE observation ID: PSP\_007272\_1945).

90, 180, and 270 degrees and the resultant images are also used as positive samples.

After sample data collection, the next step is to extract features to train the classifier. We adopt two types of features to characterize the small new crater. The first feature is the local binary patterns (LBP) feature (Ojala et al., 1996). LBP is a powerful texture descriptor that can be extracted and classified with a low-computational complexity. The original LBP operator labels the pixels of an image by thresholding the  $3 \times 3$  neighborhood of each pixel with the center value and the result is coded as a binary string (i.e. if the pixel value is larger than the center value, the pixel is coded as 1, and otherwise it is coded as 0). Fig. 6 is an example of the basic LBP operator. Later, a multi-scale LBP operator using neighborhoods of different sizes was developed (Ojala et al., 2002) to solve the problem that features calculated in  $3 \times 3$  neighborhood cannot capture large scale structure. In multi-scale LBP, circular neighborhoods are used. This operator can be set to any radius and pixel numbers in the neighborhood. Another extension to the basic LBP is to use uniform patterns which contain at most two bitwise 0 to 1 or 1 to 0 transitions in the circular presentation of the binary string. For example, 00000000 or 10001111 are the uniform patterns, while 10101000 having five transitions is not the uniform pattern. The uniform LBP feature reduces the length of the feature vector and enables rotation invariance (Ojala et al., 2002). In our research, we use a multi-scale uniform LBP ( $LBP_{P,R}^{u2}$ ,

where P represents the sampling points, R is the circle radius and superscript u2 stands for using uniform patterns) feature which combines multi-scale LBP and uniform LBP with a radius of two pixels (corresponding to a window of  $5 \times 5$  pixels) and eight pixels in the neighborhood. In the end, a total of 59 features are obtained for each resized sample.

The second feature is a Haar-like feature which was first described by Papageorgiou et al. (1998), and a generalization of Haar-like feature (Viola and Jones, 2001) that has been used in crater detection by machine learning (Bandeira et al., 2012; Di et al., 2014a, 2014b; Martins et al., 2009). A Haar-like feature represents the differences in average intensities between different regions. To calculate the Haar-like feature, a window of a mask size is moved over the input image. The Haar-like feature is represented by a row vector with each element being the value of a convolution result. Since the small crater samples are round and usually have a shadow boundary, we only use five square masks (Fig. 7) to reduce the number of Haar-like features. In the masks, the black region and white region of the mask respectively stands for -1 and +1, and the region outside the mask stands for 0. The training images are traversed by each mask of Haar-like feature, and the feature values are calculated for each pixel through convolution. The original size of the first two and the last masks in Fig. 7 is  $2 \times 2$  pixels, and that of the third and fourth masks is  $3 \times 3$  pixels. Then the size of the masks

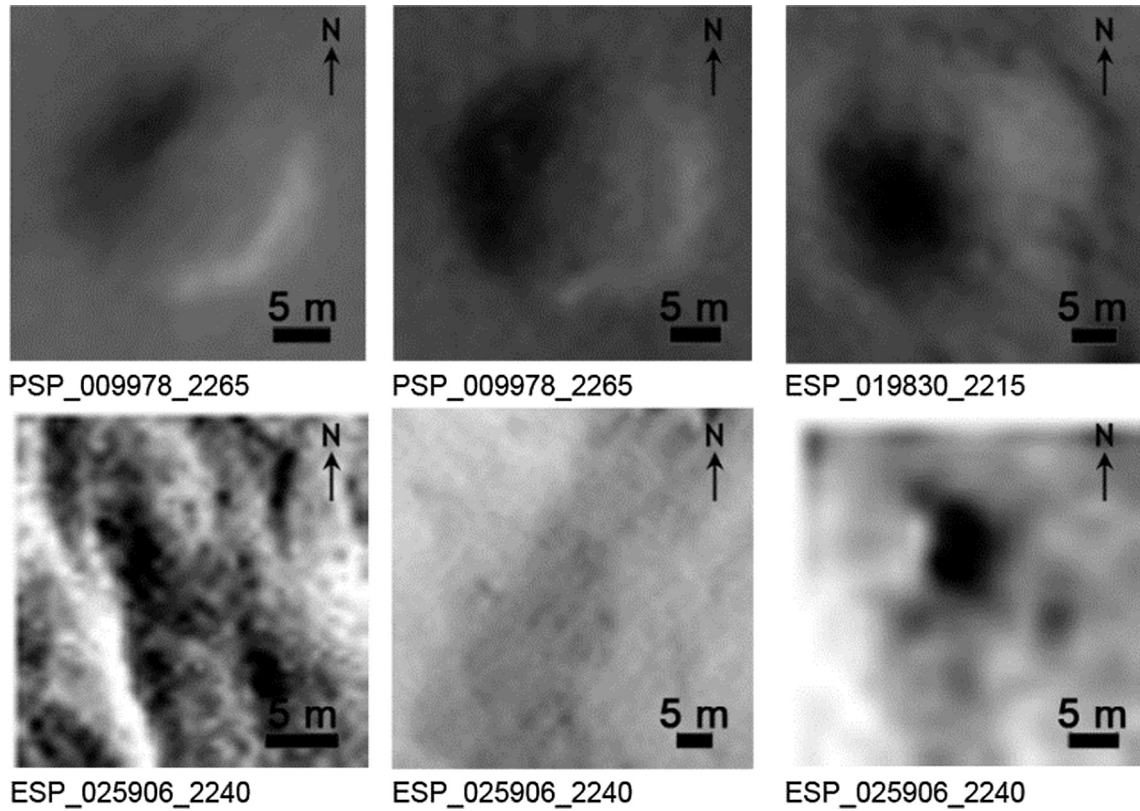


Fig. 5. Examples of positive samples (the first row) and negative samples (the second row) from HiRISE (enlarged from  $15 \times 15$  pixels). HiRISE observation IDs are indicated below each subfigure.

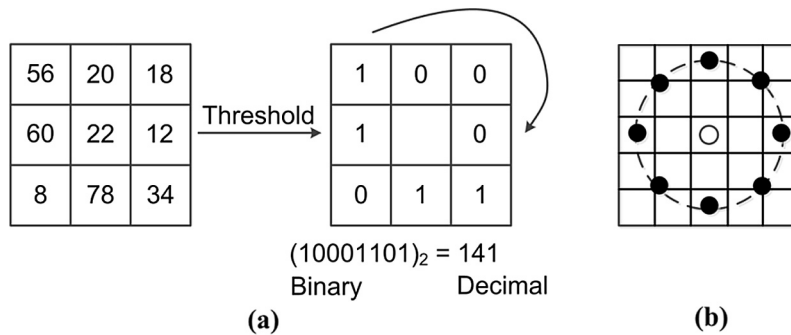


Fig. 6. LBP operator. (a) Basic LBP operator. The numbers in the left square are the DN values of the pixel. The binary string 10001101 is acquired by clockwise coding the thresholding result from the top left corner. (b) Multi-scale uniform LBP operator ( $R = 2$ ).



Fig. 7. Five square masks used for computing Haar-like feature.

is doubled, tripled, quadrupled until the mask is larger than the size of the sub-image ( $15 \times 15$  pixels). As a result, 2350 features for each resized sample are obtained. Although the

number of the Haar-like features is quite large, the computation can be very fast by using the integral image (Lienhart and Maydt, 2002; Viola and Jones, 2001).

### 3.3. AdaBoost classifier training

With a feature set extracted from the positive and negative samples, as we have introduced in the previous section, many machine learning approaches, such as decision trees and neural networks, can be used to derive a binary classifier. However, the number of features extracted is far larger than eventually needed, and computation with the over-complete set is much more expensive. With the aim of selecting the best features and training the classifier simultaneously, we choose a classification algorithm based on the variant of AdaBoost proposed by Viola and Jones (2004). This algorithm can automatically select the most useful features. In this study, a cascade classifier which combines two individual classifiers (LBP classifier and Haar-like classifier) is introduced. The individual classifiers are constructed first and the results which satisfy both of the individual classifiers are outputted as the result of the cascade classifier.

According to the very small number of features, every weak classifier which is formed in each iteration loop is constructed by only a single rectangle feature which can separate the positive and negative samples best (Martins et al., 2009; Viola and Jones, 2004). Each weak classifier  $h(x, f, p, \theta)$  is based on the following thresholding operation:

$$h(x, f, p, \theta) = \begin{cases} 1, & \text{if } p \cdot f(x) \geq p \cdot \theta \\ 0, & \text{otherwise} \end{cases} \quad (3)$$

where  $x$  is an image block to be classified,  $f(x)$  is the numerical value of a specific feature to  $x$ ,  $\theta$  is a threshold, and  $p \in \{-1, 1\}$  is a polarity variable indicating the direction of the inequality. The result 1 and 0 represent positive (crater) and negative (non-crater), respectively. In practice, each weak classifier by itself performs with a high error rate, because no single feature has a high ability of classification. However, different features reflect different aspects of the classification between craters and non-craters. Thus, the weak classifiers are combined in the end to form an effective classifier which can be stronger and well-performing. In this algorithm, the boosting selects one feature from all the potential features per iteration. The main steps are briefly described as follows (Viola and Jones, 2004):

- (1) Using training images  $(x_1, y_1), \dots, (x_n, y_n)$ , where  $y_i = 1, 0$  for positive and negative class, respectively. Extract all feature vectors from each block for the training images.
- (2) Initialize the weight  $w_{1,i}$  for each training image  $i$  as follows:

$$w_{1,i} = \begin{cases} \frac{1}{2m}, & \text{if } i \text{ is positive} \\ \frac{1}{2l}, & \text{if } i \text{ is negative} \end{cases} \quad (4)$$

where  $m$  is the number of positive samples and  $l$  is the number of negative samples in the training set.

- (3) Run the training iteratively. For  $t = 1, \dots, S$  ( $S$  is the desired number of weak classifiers), the following steps are performed:

- (a) Normalize the weights with the following equation:

$$w_{t,i} = \frac{w_{t,i}}{\sum_{j=1}^n w_{t,j}} \quad (5)$$

where  $n$  is the number of training images,  $j$  is the sequence number of the training image.

- (b) Calculate the weighted error  $E_t$  with respect to  $w_t$  as follows:

$$E_t = \sum_i w_{t,i} |h(x_i, f, p, \theta) - y_i| \quad (6)$$

- (c) Select the classifier  $h_t(x)$  with the minimum error  $\varepsilon_t = \min_{f,p,\theta} E_t$
- (d) Update the weights  $w_{t,i}$  as follows:

$$w_{t+1,i} = w_{t,i} \cdot \beta_t^{1-e_i} \quad (7)$$

where  $e_i = 0$  if the image block  $x_i$  is classified correctly,  $e_i = 1$  otherwise, and  $\beta_t = \varepsilon_t / (1 - \varepsilon_t)$ .

- (4) Combine the outputs of all weak classifiers to build a final strong classifier with the following equation:

$$H(x) = \begin{cases} \text{positive, if } R > 0 \\ \text{negative, otherwise} \end{cases} \quad (8)$$

where

$$R = \sum_{t=1}^S \alpha_t \cdot h_t(x) - \frac{1}{2} \sum_{t=1}^S \alpha_t, \alpha_t = \log\left(\frac{1}{\beta_t}\right) \quad (9)$$

The sign of the classification result  $R$  represents the class, while the absolute magnitude of  $R$  represents the “confidence” of the classification. To regulate the false positive rate (FPR) and false negative rate (FNR), a bias term  $T$  is introduced and take the sign of  $(R-T)$  to decide the class eventually. If  $(R-T) > 0$ , the class is determined as positive, and the class is determined as negative otherwise. Increasing  $T$  not only decreases the FPR but also increases the FNR. The performance of the boosting classifier algorithm is evaluated through the calculation of true positive rate (TPR) and FPR, given by the following formulas:

$$\text{TPR}(\%) = \frac{\text{TP}}{\text{TP} + \text{FN}} \times 100 \quad (10)$$

$$\text{FPR}(\%) = \frac{\text{FP}}{\text{FP} + \text{TN}} \times 100 \quad (11)$$

where TP is the number of true positives, FN is the number of false negatives, FP stands for the number of false positives, and TN is the number of true negatives. TP, TN, FN and FP are all evaluated manually based on the ground truth.

In addition to TPR and FPR, the detection rate (DR) is also used to evaluate the overall performance of the method. The detection rate is given by the following formula:

$$DR(\%) = \frac{TP + TN}{TP + FN + FP + TN} \times 100 \quad (12)$$

The larger DR is, the better the overall performance.

Classifiers using LBP and Haar-like features, individually, can generate different FPR results. For example, the LBP classifier sometimes gives a false result by considering non-crater regions as small craters in flat areas, while the Haar-like classifier produces similar mistakes in non-flat areas. Constructing a cascade of the two classifiers can generate more reliable result with less FPR. Only the regions that are detected by both LBP and Haar-like classifiers as craters are considered to be the final positive results. In this cascade scheme, a large number of negative samples can be eliminated using the LBP classifier, and additional negatives are eliminated using the Haar-like classifier. Although the classification with a cascade classifier and that with parallel individual AdaBoost classifiers have the same results, the cascade classifier imports less test samples in the second classifier (the Haar-like classifier in our case), which not only increases the detection performance but also reduces the computation time.

### 3.4. New impact site detection

New impact craters in the dark areas have different sizes. In order to detect objects of different sizes, two approaches have been proposed: resizing the images or resizing the detection blocks (Yue et al., 2008). We choose the first approach in this study.

The dark areas (new impact site candidates) are resized by building a pyramid of four scales. The size of each scale is decreased to 0.6 times the size of the previous scale. The original dark area image is in the bottom scale of the pyramid. A cascade classifier window then slides across each of these images to determine new impact crater regions. So in each scale, a  $15 \times 15$  pixels' square window is slid by three pixels each time to scan the dark areas. As a result, the dark areas are classified as new impact crater areas or non-new impact crater areas.

Due to the sliding window and multiple scales in crater detection, a small crater inside the dark area may be detected multiple times by slightly different windows at the same scale or different scales. Thus, it is necessary to check the positions of the detected new impact crater regions and delete the repeated ones. To do this, the position, height and width of every new impact crater region in the original image are stored and compared using the following formulas:

$$\text{abs}(x_1 - x_2) \leq \frac{\max(w_1, w_2)}{4} \quad (13)$$

$$\text{abs}(y_1 - y_2) \leq \frac{\max(h_1, h_2)}{4} \quad (14)$$

$$\frac{\min(w_1, w_2)}{\max(w_1, w_2)} \geq 0.5 \quad (15)$$

where  $x, y$  are the coordinates of the center, and  $w, h$  are the width and height of the new impact crater region. Eq. (13) and Eq. (14) are employed to detect position similarity and Eq. (15) is adopted to detect size closeness. If two regions satisfy all the formulas above, they are considered as repeated regions. The region with the maximum value of  $R$  is considered as the new impact crater region, and the other regions are filtered out.

## 4. Experimental results and discussion

In this research, we have developed the new impact site candidate detection method based on Matlab, and employed the Graphics and Media Lab (GML) AdaBoost toolbox (Vezhnevets, 2009) to train the cascade classifier and extract the new impact sites. One-hundred HiRISE images have been utilized to test the performance of the method.

### 4.1. AdaBoost classifier training

We randomly extracted 1105 negative samples and 636 positive samples (159 original samples and 477 rotated ones) from 32 HiRISE images. Each training sample is characterized by 2409 features (59 LBP features and 2350 Haar-like features). A small subset of features which are considered to be more effective for classification is extracted through the boosting algorithm. Fig. 8 shows the top eight Haar-like mask-features selected by AdaBoost from the training set. All the eight features are shown on the same gray scale image block. Since small craters have obvious edges and appear as a pair of shadow and illumination semicircle areas, most of the features are located at the edges or the dividing line of the shadow, so that they can effectively match the characteristics of the small craters.

The accuracy curves of LBP and Haar-like classifiers for the training set are shown in Fig. 9. The Haar-like classifier achieves an accuracy of nearly 0.87 while the LBP classifier is nearly 0.75 even with only one feature. The Haar-like and LBP classifiers can correctly distinguish all the samples

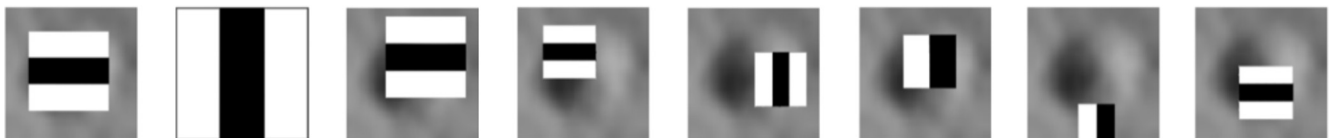


Fig. 8. Top eight Haar-like features selected by AdaBoost using the training set.

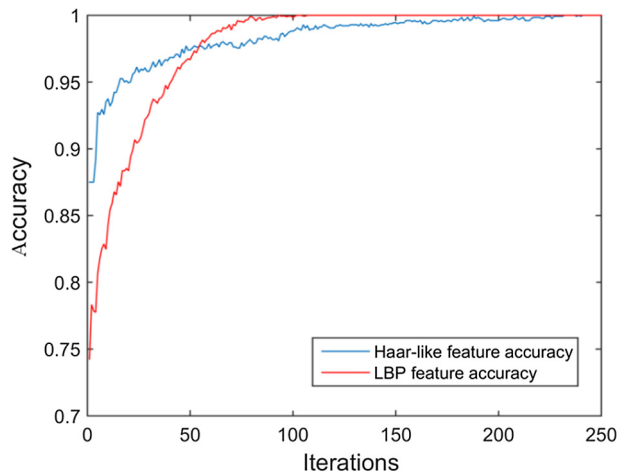


Fig. 9. Accuracy curves of LBP and Haar-like classifiers of the training set.

when the iteration number reaches 240 and 100, respectively. Although both of the two classifiers can separately perform well in classifying the samples in the training set, the FPR is high when we individually apply the features to detect craters in the images. The cascade classifier aims to perform better than both classifiers. In order to compare the performances of the two single-feature classifiers and the cascade classifier, the receiver operating characteristic (ROC) curves are generated and shown in Fig. 10. The ROC curves prove that the cascade classifier always performs better than the other two single-feature classifiers. The cascade classifier can achieve a higher TPR and a lower FPR than the other two classifiers while maintaining the same FPR or TPR.

The boosting classifier is also evaluated using tenfold cross-validation. It means that the whole set of samples is divided into ten subsets with the same size, and nine of them are used for training, the one left is used for testing. This is repeated for ten times, and each subset can be used once for testing. The average accuracy of cross-validation

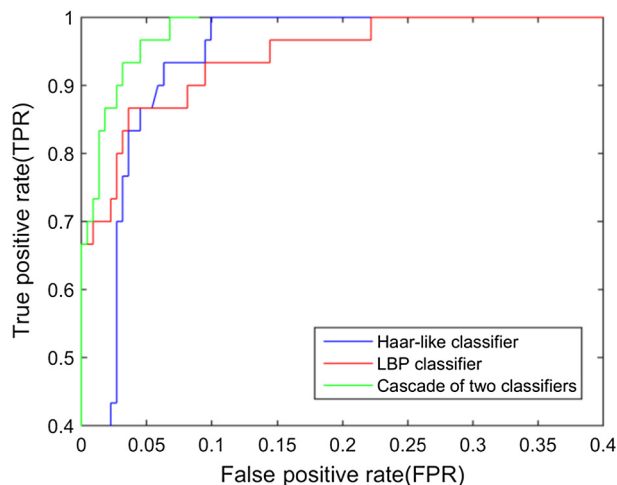


Fig. 10. ROC curves of the two classifiers and the cascade classifier of cross-validation data.

in individual LBP and Haar-like classifiers is 93.75% and 91.69%, respectively, while the cascade AdaBoost classifier can achieve an average accuracy of 95.4%. The results of cascade AdaBoost classifiers are better than that of individual classifiers with the same parameters.

It should be noted that the iteration number and bias term  $T$  can affect the training result. We constructed the cascade classifier through adjusting the bias term  $T$  to change the TPR and FPR. With several comparative experiments, for the cascade classifier, the iteration number of LBP classifier is set at 120, bias term  $T$  is set at 0, and the iteration number of Haar-like classifier is set at 200 and 0.2, respectively.

#### 4.2. New impact site detection results

In the step of new impact site candidates detection, 3219 dark areas have been detected for the subsequent AdaBoost learning. Out of 409,595 dark areas are detected after opening and closing operations, 16,887 dark areas are left after small area elimination (392,708 areas are deleted), 6737 dark areas are left after narrow and long dark areas elimination (10,150 areas are deleted), and 3219 dark areas are left after bright-dark area matching (3518 areas are eliminated).

According to the terrain relief within the regions, the experimental regions are divided into flat regions and non-flat regions. Figs. 11 and 12 show typical examples of the experimental results in flat regions and non-flat regions, respectively. In Fig. 11, it is easy to find that new impact sites can be well identified in flat regions, and most of the detected small craters are correct. In non-flat regions, some rocks (Fig. 12a, c) and small topographic features (Fig. 12a, d) affected small crater detection and resulted in false positive results. With the help of the reported locations of the new impact sites, we manually select 122 new impact sites from the 100 images and use them as ground truth. Table 1 shows the statistics of the detection results. One hundred and six dark areas which contain new impact craters are detected. The performance of our method in all regions are DR = 84.5%, TPR = 86.9%, and FPR = 15.6%. All of the indexes in flat regions (DR = 93.0%, TPR = 91.5%, FPR = 7.0%) are notably better than those in non-flat regions (DR = 76.0%, TPR = 77.5%, FPR = 24.0%). The results indicate that this method can effectively identify the new impact sites especially in flat regions.

As shown in Table 1, the DR and TPR in flat regions are higher than that in non-flat regions, and the FPR in flat regions is much lower than that in non-flat regions. By examining the false positive regions in the detection results (e.g., as the non-flat regions shown in Fig. 12), we find that there are mainly two reasons of the higher FDR in non-flat regions. The first cause is that shadow area caused by large topography relief (e.g., mountain ridges) is extracted as a new impact site candidate. The second cause is that some rocks and topographic features have similar features as

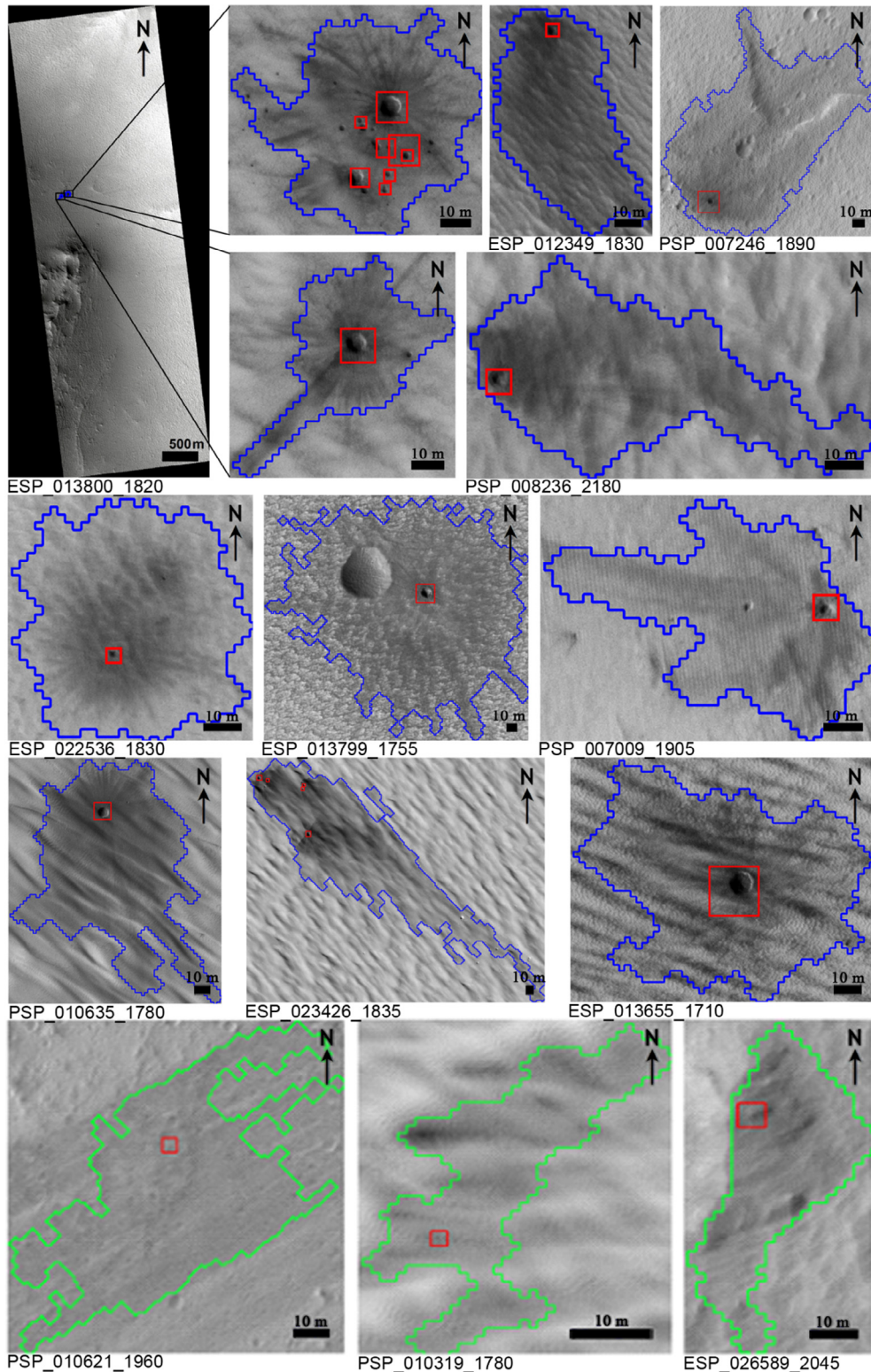


Fig. 11. Typical experimental results in flat regions in a HiRISE image. The blue lines are the boundaries of the detected new impact sites, and the green lines are the boundaries of the false positive regions. Red rectangles represent the detected small craters. HiRISE observation IDs are indicated below each subfigure. (For interpretation of the references to colour in this figure legend, the reader is referred to the web version of this article.)

small craters; for example, all of them have obvious edges and both the rocks and small craters have illuminated and shadow areas. Co-existence of both causes would result in false positive results. In the future, we will try to reduce

FPR in new impact crater detection, especially in non-flat regions by considering the illumination angle of the image and the texture information inside the new impact site candidate. Although illumination angle has been used in delet-

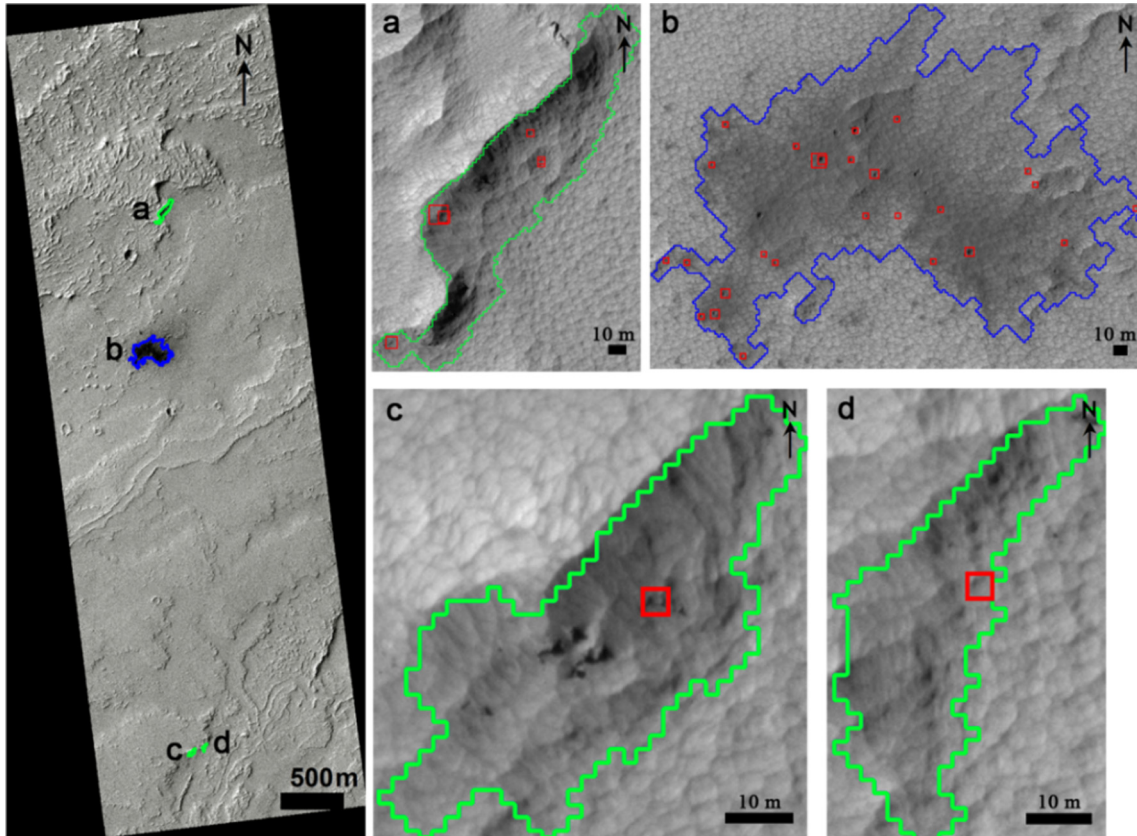


Fig. 12. Typical experimental results in non-flat regions in a HiRISE image. The blue line is the boundary of the correctly detected new impact sites, and the green lines are the boundaries of the false positive regions. Red rectangles represent the detected small craters. (HiRISE observation ID: PSP\_010292\_1785). (For interpretation of the references to colour in this figure legend, the reader is referred to the web version of this article.)

Table 1  
Statistics of the detection results.

Region type	Number of dark areas	Number of new impact sites	Detection rate (%)	True positive rate (%)	False positive rate (%)
All regions	3219	122	84.5	86.9	15.6
Flat regions	1619	82	93.0	91.5	7.0
Non-flat regions	1600	40	76.0	77.5	24.0

ing possible shadows in dark areas, it is more difficult to use illumination angle in small craters which only cover a few pixels. The potentials will be investigated in the future.

### 4.3. Discussion

In this study, we have developed a new impact sites detection method. New impact site candidates are extracted through dark area detection algorithm first. Then new impact craters are detected through a classifier trained by AdaBoost. The detected minimum and maximum sizes of the new impact crater are 9 pixels and 80 pixels, respectively. And the average size of the extracted new impacted craters is 17 pixels. As our method first extracts new impact site candidates through dark area detection, the method is more suitable for dust-mantled regions where the ejecta of new impact craters is dark. In the literature, the most documented new impact craters are in the dust-mantled region and have dark blast zones. There are also a very small por-

tion of new impact craters that have light-toned blast zones. In our experiment, the bright areas which are formed in non-dusty regions cannot be detected. There are not enough samples which are formed in non-dusty regions can be found, because the new impact sites in non-dusty areas are hard to identify by manual work and only few sites have been found. Therefore, our method is not suitable to detect new impact sites in non-dust-mantled regions. In the future, if more new impact sites in non-dust-mantled regions are discovered, extensional work on studying their characteristics and automatically detecting both types of new impact sites would be implemented.

The parameters of the algorithms have been selected through theoretical analysis and comparative experiments. In the step of dark area detection, all of the images are pre-processed by histogram equalization, and the two thresholds ( $T1 = 60$ ,  $T2 = 90$ ) are selected according to the best comparative results (largest number of the dark areas that actually contain new impact sites). In order to eliminate

narrow and shadow areas, we set a size ratio threshold and an angle threshold, which give reliable results. In the step of machine learning, the number of scales and scale step size are set based on the size of the largest crater and the size of the window. The reliability of the parameters for the LBP classifier and Haar-like classifier are verified through good results of cross-validation. The same set of parameters has been applied to all the images in the experiment, and they should be applicable to other new HiRISE images.

So far, identification of fresh craters has been commonly done using pairs of images (before and after the new crater is formed) and using change detection techniques. With the proposed method, it is possible to detect new impact sites in single high resolution images. This may bring benefits of finding more new impact sites from high resolution images without depending on the previous images of the same region, especially when “previous images” are not available or not of enough resolution.

At this stage, this automated method cannot completely substitute for manual interpretation. But when large amounts of high-resolution images are acquired by current and future missions, it could be a useful tool to prescreen new impact sites to significantly reduce manual work. For prescreening purposes, we can detect all the new impact sites while allowing high FPR through adjusting the relevant thresholds. Ultimately, the results of the automated method should be confirmed by experts. If there are repeated observations of before and after impacts, the detected new impact sites can be confirmed and dated. And if there is no repeated observation, our method can still offer assistance in detecting new impact sites.

## 5. Conclusions

In this study, an automatic detection method has been presented to detect new Martian impact sites using HiRISE images. First, a pixel-based method was introduced to detect candidate sites in the whole image through dark area detection and morphological processing. Then, a cascade AdaBoost classifier was constructed based on a combination of scaled LBP and Haar-like features to identify new small craters so as to distinguish new impact sites from non-new impact sites. Experimental results using 100 HiRISE images showed that the proposed method can achieve good performance, especially in flat regions. The overall detection rate for all regions is 84.5%, true positive rate is 86.9%. The detection rate and true positive rate in flat regions are 93.0% and 91.5%, respectively. Future research will focus on accuracy improvement in non-flat regions and improving the efficiency of the classifier.

## Appendix A.

HiRISE images used in the experiment. Test images: serial number from 1 to 100. Training images: serial number from 101 to 132.

Serial number	HiRISE observation ID	Serial number	HiRISE observation ID
1	PSP_007246_1890	2	PSP_010635_1780
3	PSP_006998_2060	4	ESP_016200_1740
5	PSP_007272_1945	6	ESP_012349_1830
7	PSP_007496_1735	8	ESP_013707_1915
9	PSP_010528_1770	10	ESP_017969_1855
11	PSP_010621_1960	12	ESP_016149_1905
13	PSP_010319_1780	14	ESP_015949_1795
15	ESP_016331_1730	16	ESP_016582_1760
17	ESP_023426_1835	18	ESP_025943_1850
19	ESP_026589_2045	20	ESP_017038_1790
21	ESP_017481_2110	22	ESP_018404_1775
23	ESP_018784_2050	24	ESP_017229_2110
25	ESP_018217_1645	26	ESP_017927_1875
27	ESP_018493_1925	28	ESP_018707_2205
29	ESP_018854_2270	30	ESP_022536_1830
31	ESP_020869_1990	32	ESP_020714_2125
33	ESP_022056_1925	34	ESP_022964_1845
35	ESP_025864_1835	36	ESP_028659_2050
37	ESP_026009_1920	38	ESP_026038_2155
39	ESP_027975_1835	40	ESP_026221_1825
41	PSP_007378_1860	42	PSP_004689_1765
43	PSP_004123_1915	44	PSP_008300_1905
45	PSP_003075_2020	46	PSP_003754_1815
47	ESP_017808_1755	48	PSP_002736_2075
49	PSP_004175_2060	50	ESP_013800_1820
51	ESP_016344_1825	52	ESP_011425_1775
53	ESP_017389_1690	54	PSP_003101_2065
55	PSP_003925_1940	56	ESP_012375_2035
57	PSP_007009_1905	58	PSP_004414_1850
59	PSP_003780_2000	60	ESP_013799_1755
61	PSP_003602_2085	62	PSP_003527_1940
63	PSP_003172_1870	64	ESP_017030_1755
65	ESP_016559_1855	66	ESP_027316_1810
67	PSP_009185_1770	68	ESP_013655_1710
69	PSP_010147_1830	70	ESP_011618_1885
71	PSP_007879_1725	72	ESP_028979_1730
73	PSP_010547_2195	74	PSP_007561_1290
75	PSP_007596_1295	76	ESP_016465_1735
77	ESP_011716_2100	78	ESP_013640_2055
79	PSP_007773_1930	80	PSP_010177_1850
81	ESP_016660_1860	82	PSP_010331_1755
83	ESP_016793_1855	84	ESP_022912_1720
85	ESP_022279_1690	86	PSP_008015_2205
87	PSP_008045_2020	88	ESP_022299_2040
89	PSP_008236_2180	90	PSP_010292_1785
91	ESP_024349_2020	92	PSP_010862_1880
93	PSP_009212_1640	94	ESP_011491_2090
95	PSP_009305_1830	96	ESP_014150_2130
97	PSP_010861_2265	98	ESP_011295_2205
99	ESP_011781_2100	100	ESP_013893_1755
101	ESP_022964_1845	102	ESP_025840_2240
103	PSP_010740_1840	104	PSP_010084_2235
105	PSP_010634_2135	106	ESP_017231_1880

107	ESP_012047_1755	108	PSP_010255_1700
109	ESP_011584_1785	110	PSP_010585_2255
111	ESP_011368_1860	112	ESP_016115_2010
113	ESP_011698_1810	114	PSP_009978_2265
115	ESP_019830_2215	116	ESP_013590_1625
117	ESP_024211_2060	118	ESP_012441_1775
119	ESP_014168_1920	120	ESP_026960_1710
121	PSP_010200_1805	122	ESP_014010_1800
123	ESP_029015_1705	124	ESP_013788_1910
125	ESP_013161_1715	126	ESP_018586_1735
127	ESP_016648_1665	128	ESP_027410_1740
129	ESP_018019_1735	130	ESP_013629_1740
131	ESP_020855_2035	132	ESP_014143_1950

## References

- Bandeira, L., Saraiva, J., Pina, P., 2007. Impact crater recognition on Mars based on a probability volume created by template matching. *IEEE Trans. Geosci. Remote Sens.* 45 (12), 4008–4015.
- Bandeira, L., Ding, W., Stepinski, T.F., 2012. Detection of sub-kilometer craters in high resolution planetary images using shape and texture features. *Adv. Space Res.* 49 (1), 64–74.
- Byrne, S., Dundas, C.M., Kennedy, M.R., Mellon, M.T., Mcewen, A.S., Cull, S.C., Daubar, I.J., Shean, D.E., Seelos, K.D., Murchie, S.L., Cantor, B.A., Arvidson, R.E., Edgett, K.S., Reufer, A., Thomas, N., Harrison, T.N., Posiolova, L.V., Seelos, F.P., 2009. Distribution of mid-latitude ground ice on Mars from new impact craters. *Science* 325 (5948), 1674–1676.
- Calef III, F.J., Herrick, R.R., Sharpton, V.L., 2009. Geomorphic analysis of small rayed craters on Mars: examining primary versus secondary impacts. *J. Geophys. Res.* 114 (E10007).
- Daubar, I.J., Mcewen, A.S., Byrne, S., Kennedy, M.R., Ivanov, B., 2013. The current Martian cratering rate. *Icarus* 225 (1), 506–516.
- Daubar, I.J., Mcewen, A.S., Byrne, S., Kreslavsky, M., Saper, L., Kennedy, M.R., 2014. New dated impacts on Mars and an updated current cratering rate. In: *Eighth International Conference on Mars*, 14–18 July 2014, California, United States, pp. 1007.
- Daubar, I.J., Dundas, C.M., Byrne, S., Geissler, P., Bart, G.D., Mcewen, A.S., Russell, P.S., Chojnacki, M., Golombek, M.P., 2016. Changes in blast zone albedo patterns around new Martian impact craters. *Icarus* 267, 86–105.
- Di, K., Li, W., Yue, Z., Sun, Y., Liu, Y., 2014a. A machine learning approach to crater detection from topographic data. *Adv. Space Res.* 54 (11), 2419–2429.
- Di, K., Liu, Y., Hu, W., Yue, Z., and Liu, Z., 2014. Mars surface change detection from multi-temporal orbital images, *ISRSE35*, 22–26 April 2013, Beijing, China, pp. 682–691.
- Dundas, C.M., Byrne, S., McEwen, A.S., Mellon, M.T., Kennedy, M.R., Daubar, I.J., Saper, L., 2014. HiRISE observations of new impact craters exposing Martian ground ice. *J. Geophys. Res.* 119 (1), 109–127.
- Golombek, M., Robinson, K., McEwen, A., Bridges, N., Ivanov, B., Tornabene, L., Sullivan, R., 2010. Constraints on ripple migration at Meridiani Planum from Opportunity and HiRISE observations of fresh craters. *J. Geophys. Res.* 115 (E00F08), 129–143.
- Jin, S., Zhang, T., 2014. Automatic detection of impact craters on Mars using a modified adaboosting method. *Planet. Space Sci.* 99, 112–117.
- Kim, J.R., Muller, J.P., Gasselt, S.V., Morley, J.G., Neukum, G. the HRSC Col Team, 2005. Automated crater detection, a new tool for Mars cartography and chronology. *Photogramm. Eng. Rem. Sens.* 71 (10), 1205–1217.
- Lienhart, R., and Maydt, J., 2002. An extended set of Haar-like features for rapid object detection. *IEEE Icip*, 1: 900–903.
- Malin, M.C., Edgett, K.S., Posiolova, L.V., McColley, S.M., Noe Dobrea, E.Z., 2006. Present-day impact cratering rate and contemporary gully activity on Mars. *Science* 314, 1573–1577.
- Malin, M.C., Bell III, J.F., Cantor, B.A., Caplinger, M.A., Calvin, W.M., Clancy, R.T., Edgett, K.S., Edwards, L., Haberle, R.M., James, P.B., Lee, S.W., Ravine, M.A., Thomas, P.C., Wolff, M.J., 2007. Context camera investigation on board the Mars reconnaissance orbiter. *J. Geophys. Res.* 112, E05S04.
- Malin, M.C., Edgett, K.S., Cantor, B.A., Caplinger, M.A., Danielson, G. E., Jensen, E.H., Ravine, M.A., Sandoval, J.L., Supulver, K.D., 2010. An overview of the 1985–2006 Mars Orbiter Camera science investigation. *Int. J. Mars Sci. Explor.* 5, 1–60.
- Martins, R., Pina, P., Marques, J.S., Silveira, M., 2009. Crater detection by a boosting approach. *IEEE Geosci. Remote Sens. Lett.* 6 (1), 127–131.
- Mcewen, A.S., Eliason, E.M., Bergstrom, J.W., Bridges, N.T., Hansen, C. J., Delamere, W.A., Grant, J.A., Gulick, V.C., Herkenhoff, K.E., Keszhelyi, L., Kirk, R.L., Mellon, M.T., Squyres, S.W., Thomas, N., Weitz, C.M., 2007. Mars reconnaissance orbiter's High Resolution Imaging Science Experiment (HiRISE). *J. Geophys. Res.*, 112, E05S02
- Ojala, T., Pietikäinen, M., Harwood, D., 1996. A comparative study of texture measures with classification based on feature distributions. *Pattern Recogn.* 29 (1), 51–59.
- Ojala, T., Pietikäinen, M., Mäenpää, Topi., 2002. Multiresolution gray-scale and rotation invariant texture classification with local binary patterns. *IEEE Trans. Pattern Anal. Mach. Intell.* 24 (7), 971–987.
- Papageorgiou, C.P., Oren, M., Poggio, T., 1998. A general framework for object detection. In: *Washington, D.C. (Ed.), Proceedings of the Sixth International Conference on Computer Vision*, 4–7 January 1998, Washington, DC, United States, pp. 555–562.
- Salamunićar, G., Lončarić, S., Pina, P., Bandeira, L., Saraiva, J., 2011. MA130301GT catalogue of Martian impact craters and advanced evaluation of crater detection algorithms using diverse topography and image datasets. *Planet. Space Sci.* 59, 111–131.
- Salamunićar, G., Lončarić, S., Grumpe, A., Wöhler, C., 2014. Hybrid method for crater detection based on topography reconstruction from optical images and the new LU78287GT catalogue of Lunar impact craters. *Adv. Space Res.* 53, 1783–1797.
- Sawave, Y., Matsunaga, T., Rokugawa, S., 2006. Automated detection and classification of lunar craters using multiple approaches. *Adv. Space Res.* 37, 21–27.
- Serra, J., 1982. *Image Analysis and Mathematical Morphology*. Academic Press, pp. 50–55.
- Urbach, E.R., Stepinski, T.F., 2009. Automatic detection of sub-km craters in high resolution planetary images. *Planet. Space Sci.* 57, 880–887.
- Vezhnevets, A., GML AdaBoost matlab toolbox. <<http://graphics.cs.msu.ru/ru/science/research/machinelearning/adaboosttoolbox>> (accessed on 1 February, 2009).
- Viola, P., Jones, M., 2001. Rapid object detection using a boosted cascade of simple features. *Comput. Vision Pattern Recog. (CVPR)* 1, 511–518.
- Viola, P., Jones, M.J., 2004. Robust real-time face detection. *Int. J. Comput. Vision* 57 (2), 137–154.
- Wagstaff, K.L., Panetta, J., Ansar, A., Greeley, R., Hoffer, M.P., Bunte, M., Schögrhofer, N., 2012. Dynamic landmarking for surface feature identification and change detection. *ACM Trans. Intell. Syst. Technol.* 3 (3), 49.
- Williams, J., Pathare, A.V., Aharonson, O., 2014. The production of small primary craters on Mars and the Moon. *Icarus* 235, 23–36.
- Yue, Z.Y., Liu, J.Z., Wu, G.G., 2008. Automated detection of lunar craters based on object-oriented approach. *Chin. Sci. Bull.* 53 (23), 3699–3704.
- Zurek, R.W., Smrekar, S.E., 2007. An overview of the Mars Reconnaissance Orbiter (MRO) science mission. *J. Geophys. Res. Planets*, 112, E05S01.